

ASEAN Journal of Science and Engineering



Journal homepage: http://ejournal.upi.edu/index.php/AJSE/

Sustainable Liquid-Phase Alkylation of Toluene Using Zeolitic Catalysts: A Comparative Evaluation of Al-Rich Y and Si-Rich Beta Zeolites for Industrial Green Chemistry to Support Sustainable Development Goals (SDGs)

Samaa H. Al-Sultani¹, Ali Al-Shathr^{1,*}, Bashir Y. Al-Zaidi¹, Zaidoon M. Shakor¹, Emad Al-Shafei²

¹Collage of Chemical Engineering, University of Technology-Iraq, Baghdad, Iraq ²Catalysts Constitute, Dhahran, Saudi Arabia

*Correspondence: E-mail: ali.r.mohammedjawad@uotechnology.edu.iq

ABSTRACT

The sustainable synthesis of linear alkylbenzenes (LABs), key intermediates for surfactants and detergents, is essential for minimizing environmental impact in the chemical industry. This study investigates the catalytic efficiency and coke deposition behavior of Al-rich Y and Si-rich Beta zeolites for the liquid-phase alkylation of toluene with 1-octene. The experiments varied temperature, catalyst loading, and timeon-stream to optimize conversion and selectivity. Al-rich Yzeolite achieved 90% of 1-octene conversion and superior monoalkyltoluene selectivity due to its higher acidity and surface area. Thermogravimetric analyses revealed distinct soft and hard coke profiles, with Y-zeolite showing slightly higher coke content. A kinetic model supported an accurate prediction of coke decomposition behavior. These findings highlight the potential of Y-zeolite as a robust, eco-friendly catalyst, aligning with sustainable development goals (SDGs) promoting sustainable catalytic processes petrochemical industries.

ARTICLE INFO

Article History:

Submitted/Received 20 Jun 2025 First Revised 24 Jul 2025 Accepted 11 Sep 2025 First Available online 12 Sep 2025 Publication Date 01 Sep 2026

Keyword:

Alkylation reactions,
Coke deactivation,
Coke kinetic modelling,
Linear alkylbenzenes (LABs),
Monoalkylated toluene,
Mono-octyl toluene,
Zeolite morphology.

© 2026 Universitas Pendidikan Indonesia

1. INTRODUCTION

Linear alkylbenzenes (LABs) are important industrial chemicals widely used in the production of surfactants, lubricant additives, plasticizers, and detergents [1,2]. The Friedel-Crafts alkylation of aromatic hydrocarbons represents a fundamental approach in many industrial processes for synthesizing alkyl aromatic compounds [3,4]. Traditionally, these alkylation reactions are carried out using alkylating agents in combination with Lewis acid catalysts such as AlCl₃ and ZnCl₂, or Brønsted acid catalysts such as HF and H₂SO₄ [5]. Currently, the majority of the 3.6 million tons of LABs produced annually are synthesized using homogeneous liquid-phase catalysts such as hydrofluoric acid (HF) or aluminum chloride (AlCl₃) [6]. However, these catalysts suffer from significant drawbacks, including environmental pollution, equipment corrosion, and challenges in product separation [7]. To overcome these limitations, the detergent industry has been actively exploring environmentally sustainable processes, particularly those employing solid acid catalysts. Heterogeneous catalysts, especially solid acids, have emerged as promising alternatives due to their favorable properties for alkylation reactions, including suitable acidity, high catalytic activity, safety in handling, and reduced environmental impact [8-11]. Zeolites and mesoporous molecular sieves are prominent examples of such environmentally friendly catalysts [12,13] and have been extensively studied in aromatic conversion processes, such as the alkylation of toluene with 1-heptene [14] and the alkylation of benzene or toluene with 1-octene [15,16]. Among the various heterogeneous catalysts, zeolites offer particularly attractive properties for catalytic applications, most notably their ability to enhance product selectivity.

A significant advancement in the industrial synthesis of ethylbenzene using solid acid catalysts was achieved by Mobil-Badger, which employed ZSM-5 zeolite in a gas-phase fixedbed reactor [17]. Following this development, various corporations refined their proprietary technologies for ethylbenzene synthesis via solid catalysts [18]. Zeolites such as ZSM-5, Y, Beta, and Mordenite have since been demonstrated to be effective solid acid catalysts for the alkylation of aromatics with olefins [8]. For industrial applications, the use of zeolite catalysts requires efficient coke regeneration while maintaining both catalytic activity and structural stability. Ensuring the stability of acidic zeolites during reactions is therefore essential. Synthetic zeolites exhibit catalytic activity through ion exchange, thermal stability, and diverse acid sites, with selectivity strongly influenced by the ratios of exchanged cations [19,20]. Among zeolites, Y-zeolite is highly porous and functions as an efficient, selective catalyst for benzene alkylation with long-chain alkenes [14,21]. Beta zeolite, which possesses smaller pores and crystal sizes than Y-zeolite, has emerged as a promising catalyst for linear alkylbenzene (LAB) synthesis [22]. While Beta zeolites display Brønsted acidity comparable to Y-zeolite, they share a common limitation with many zeolite catalysts: coke-induced deactivation [23]. Coke formation represents a major obstacle to zeolite performance, as it diminishes activity, selectivity, and long-term stability. This deactivation primarily results from coke accumulation during hydrocarbon polymerization reactions [24]. Specifically, coke blocks zeolite pores and deactivates acid sites, thereby reducing the efficiency of alkylation reactions such as the conversion of toluene with 1-olefins [25].

In the alkylation of toluene with 1-octene, various zeolite catalysts, including ZSM-5, ZSM-11, ZSM-12, Beta, Y, MCM-41, and mordenite, were employed. Micro/mesoporous composites were also explored, and catalytic activity was correlated with acidic strength in the toluene alkylation process. Zeolites with a higher density of Brønsted acid sites achieved the highest conversion rates in the alkylation reaction [26]. The synthesis of octyltoluene

using different cation-exchange resin catalysts in the liquid-phase alkylation of toluene with 1-octene has been investigated with Lewatit SP112, Amberlyst 15, and Amberlyst 35. Among these, Amberlyst 15 and Amberlyst 35 achieved conversion rates above 90%, demonstrating superior catalytic performance [27]. The effects of fresh and modified modernite and Beta zeolite catalysts on the alkylation of toluene with 1-heptene at 90 °C were studied in a batch reactor. Beta zeolite exhibited the lowest conversion due to rapid deactivation caused by coke deposition. However, dealuminated Beta zeolite improved the conversion of 1-heptene, achieving 85% in toluene alkylation. In contrast, parent mordenite zeolite demonstrated optimal selectivity, as its framework possessed a suitable pore volume that facilitated the desorption of 2-heptyl-methylbenzene isomers, leading to higher toluene alkylation conversion [25]. Enhanced conversion and selectivity in the alkylation of toluene with 1-heptene using large-pore acidic Y-zeolite have also been reported, achieving 96% conversion under a higher toluene-to-1-heptene ratio of 8:1 [8].

The selection of an appropriate zeolite catalyst for toluene alkylation is influenced by several critical factors, including pore structure and morphology, acidity, Si/Al ratio, and operating conditions such as reaction time, pressure, temperature, time-on-stream, and reactant concentration [28]. Product selectivity and catalyst deactivation due to coke deposition are also essential considerations in catalyst design and performance. Most hydrocarbon transformations occur within the microporous architecture of zeolites (comprising voids, cages, and channel intersections) rather than on the external surface [29]. Coke predominantly forms inside these micropores [30], and the degree of catalyst deactivation is directly proportional to the extent of coke accumulation. However, characterizing coke composition within zeolite structures remains challenging due to its complex nature and the difficulty of separating it from the framework [31]. Pore volume, size, and geometry significantly influence coke formation and diffusion. Zeolites with larger pores promote the formation of bulky intermediates and products but are more susceptible to extensive coke buildup. In contrast, smaller pore zeolites can suppress coke formation by restricting the mobility and entrapment of such intermediates within the pore network.

The objective of this study is to address the lack of comprehensive models for coke formation in zeolites by developing a mathematical framework to quantify both the amount and type of coke deposited on two wide-pore zeolites: aluminum-rich Y-zeolite and siliconrich Beta zeolite. Simultaneous thermogravimetric and differential thermogravimetric (TGA/DTG) analyses were employed to investigate coke deposition, and key kinetic parameters (including pre-exponential factors and activation energies for decoking) were experimentally determined. Furthermore, this study examines the influence of operating parameters and concurrent surface reactions, including 1-octene isomerization, toluene alkylation, and coke formation, on product selectivity and conversion. The integration of experimental results with kinetic modeling provides valuable insights into the multi-path reaction mechanisms occurring over zeolite catalysts and establishes a foundation for the predictive design of more stable and selective catalytic systems. The novelty of this research lies in the combined experimental and kinetic modeling approach to evaluate catalyst sustainability, which not only enhances industrial reaction performance but also supports the United Nations Sustainable Development Goals (SDGs).

2. METHODS

2.1. Materials

The chemicals used in this study were 1-octene (98%, Acros Organics), toluene (99.5%, Sigma-Aldrich), and n-pentane (99%, Scharlau). The zeolite catalysts employed were Beta and

Y in their hydrogen form, both obtained from Alfa Aesar—Thermo Fisher. All reagents and catalysts were used as received, without further purification or treatment.

2.2. Zeolite Characterization Techniques

Comprehensive characterization of the zeolite materials was conducted using several analytical techniques to evaluate their structural, morphological, chemical, and thermal properties. X-ray Diffraction (XRD) analysis was employed to identify the crystalline phases and structural composition of the zeolites, following established protocols [32]. The measurements were performed using a STOE STADI P diffractometer equipped with a Cu Kα radiation source. Scanning Electron Microscopy (SEM) was utilized to examine the surface morphology and crystal size of the zeolite samples at different magnifications [33]. A JEOL JSM-6010LA SEM equipped with Energy-Dispersive X-ray Spectroscopy (EDX) was used, and images were captured at magnifications of 2 µm and 10 µm to assess surface features and particle distribution. X-ray Fluorescence (XRF) analysis was conducted to determine the elemental composition of the zeolite catalysts, using a PANalytical Zetium XRF analyser [34]. The method is based on the detection of characteristic secondary (fluorescent) X-rays emitted from a material when it is excited by high-energy X-rays or gamma rays. The textural properties, such as specific surface area, pore volume, and pore size distribution, were determined using Brunauer-Emmett-Teller (BET) theory with a QuantaChrome Nova 2200E surface area analyser [35]. Fourier Transform Infrared Spectroscopy (FTIR) was employed to identify the functional groups present in the zeolite structure by analysing their infrared absorption spectra, using a Jasco 4200 FTIR spectrometer (Japan) [36]. Thermogravimetric Analysis (TGA) and Derivative Thermogravimetry (DTG) were used to assess the thermal stability and decomposition behaviour of the samples, carried out on a TGA Q600 instrument (TA Instruments), with data analysis performed using TA Universal Analysis software [37]. Finally, the acidity of the zeolites was evaluated through Temperature-Programmed Desorption of Ammonia (NH3-TPD) using a Micromeritics AutoChem II 2920 analyser, providing insights into the acid site strength and distribution on the catalyst surface [38].

2.3. Alkylation Reaction

The experimental procedures were conducted in a 250 mL borosilicate glass vessel equipped with a reflux condenser and immersed in an oil bath. A magnetic stirring hot plate was employed to control both temperature and stirring speed, ensuring homogeneous mixing of the reaction components, as illustrated in **Figure 1**. The alkylation reactions were performed at temperatures of 90, 100, and 110 °C under atmospheric pressure with a constant stirring rate of 200 rpm. Before the experiments, two types of zeolites (Al-rich Y-zeolite and Si-rich Beta zeolite) were activated at 200 °C for 30 min to remove moisture. The reactant mixture consisted of toluene and 1-octene in molar ratios of 3, 6, and 9, with a fixed total volume of 10 mL. Different amounts of zeolite catalysts (100, 200, and 300 mg) were used for each setup. At the end of the designated reaction time, the process was quenched by immersing the reactor in an ice bath to rapidly cool the system. The reaction mixture was then subjected to vacuum filtration using filter paper to separate the liquid phase from the zeolite catalyst for subsequent product analysis. The recovered zeolite was washed with 15 mL of n-pentane for approximately 5 min to remove any residual adsorbed species from the pore structure, followed by overnight drying.

Product and unreacted reactant concentrations were quantified using GC-FID analysis. To determine the number of moles of reactants introduced into the reactor, samples were injected into the GC-FID after being mixed with an internal standard before the reaction. All

peak areas were normalized against the known amount of the internal standard. The conversion of the limiting reactant, 1-octene, was calculated as the ratio of the moles consumed during the reaction to the initial moles present, as expressed in Equation (1).

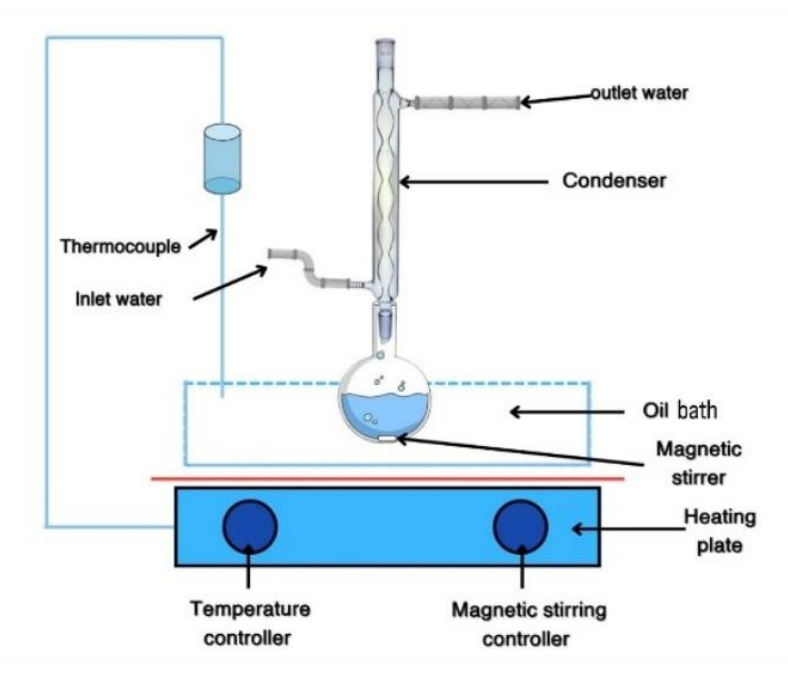


Figure 1. Batch reactor schematic for alkylation reactions.

While toluene and 1-octene were readily detected, mono-octyl toluene isomers (2-, 3-, and 4-octyl toluene) were more difficult to quantify because they are not commercially available as reference standards (see **Figure 2**). Therefore, the moles of each product were determined using a carbon number balance approach. Initially, the moles of both the starting reactants and unreacted species were established. The selectivity of all products was then calculated using Equation (2), which incorporates coke formation as one of the reaction products.

% Selectivity =
$$\left[\frac{no.of\ moles\ of\ mono-octyltoluene}{no.of\ moles\ of\ 1-octene\ consumed} \right] \times 100$$
 (2)

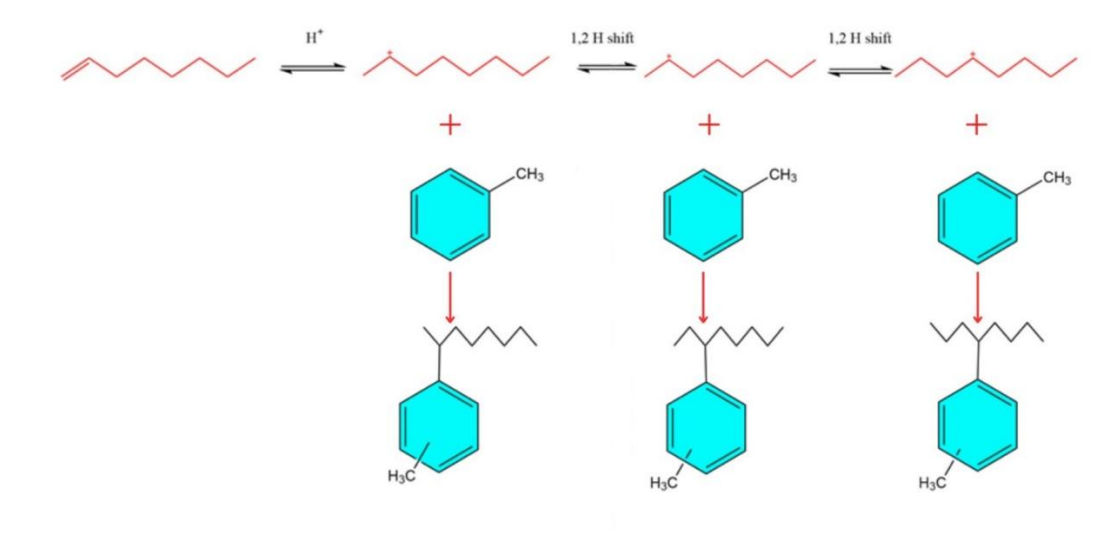


Figure 2. Scheme of alkylation of toluene with 1-octene [8].

2.4. Theoretical Section: TGA Kinetic Modelling

2.4.1. Single-step reaction (model-based method)

The model-fitting method in TGA applies various reaction kinetic models to fit the experimental TGA curves, thereby enabling the estimation of the kinetic triplet. These parameters include the pre-exponential factor, activation energy, and the kinetic model function $f(\alpha)$. However, the assumption of a single activation energy across all temperatures often poses challenges due to the complexity of solid-state reactions. The fundamental massloss rate equation, which underpins all kinetic analyses in TGA studies, is expressed in Equation (3).

$$\frac{d\alpha}{dt} = k(T)f(T) \tag{3}$$

In this equation, $f(\alpha)$ represents the reaction model, while k denotes the kinetic rate constant for the decomposition process. The temperature-dependent rate constants of the reaction model are determined using the Arrhenius equation, as shown in Equation (4). The specific reaction rate constant (k_i) for each step is defined by the following relation in Equation (4).

$$k_i(T) = A_i e^{-E_i/RT} (4)$$

In this equation, A_i (1/min) represents the pre-exponential factor, E_i (kJ/mol) is the activation energy, R is the universal gas constant with a value of 8.314 J/mol·K, and T denotes the absolute temperature. The extent of conversion, the value of α reflects the fraction of catalyst decomposed over time t, as expressed in Equation (5).

$$\alpha = \frac{m_i - m_\alpha}{m_i - m_f} \tag{5}$$

Here, m_{α} , m_i , and m_f refer to the instantaneous, initial, and final mass of the sample through the experiment, respectively. By substituting Equation (4) into Equation (5), Equation (6) is obtained.

$$\frac{d\alpha}{dt} = A_{i}f(T)e^{-E_{i}/RT} \tag{6}$$

As a result, the temperature becomes a time-dependent variable, increasing at a constant heating rate. The corresponding expression is formulated in Equation (7).

$$T = \beta t + T_0 \tag{7}$$

In this equation, the initial temperature is denoted by To, the linear heating ramp rate is represented by β , and the temperature at time t is used to indicate the temperature. The thermogravimetric analysis (TGA) experiments that employ the non-isothermal approach are carried out at a linear heating rate of β , as outlined by Equations (8) and (9) [39].

$$\beta = \frac{dT}{dt} \tag{8}$$

$$\beta = \frac{dr}{dt}$$

$$\frac{d\alpha}{dT}\frac{dT}{dt} = A_0 f(T)e^{-E_a/RT}$$
(9)

By incorporating Equation (8) into Equation (9), an approximation for Equation (10) is obtained.

$$\frac{d\alpha}{dT} = \frac{A_0}{\beta} f(\alpha) e^{-E_\alpha/RT} \tag{10}$$

The parameters Ea, R, k(T), and $f(\alpha)$ are computed based on the selected reaction model and are subsequently used to determine the activation energy, expressed in J·mol⁻¹. The kinetic differential equation applied for model-based analysis is expressed in the form of differential simulation, as shown below [40,41]. For each TGA model, an error minimization procedure using stochastic optimization is employed to accurately determine both the frequency factor and the activation energy. Each interaction model corresponds to a unique algebraic expression $f(\alpha)$ and its integral form $g(\alpha)$.

2.4.2. Multi-step reaction

When estimating the kinetic parameters of materials undergoing simultaneous multi-step reactions, both model-free and model-based approaches encounter significant challenges. Isothermal conversion methods are only applicable to single-step reactions, and their accuracy is often insufficient to fully characterize the kinetics of more complex reaction systems, thereby limiting their applicability. In contrast, multi-reaction models can more effectively capture the kinetic behavior observed in TGA, particularly for materials that exhibit a broad range of decomposition temperatures. As shown in Equation (11), the overall conversion is determined by summing the contributions of the individual conversion steps, each representing a distinct reaction [42,43].

$$\alpha = \sum_{i=1}^{N_C} C_i \alpha_i \tag{11}$$

The overall conversion rate is determined by summing the contributions of the individual conversion rates associated with each reaction step, as expressed in Equations (12) and (13).

$$\frac{d^{\alpha}}{dt} = \sum_{i=1}^{2} C_i \frac{d\alpha_i}{dt} = C_1 \frac{d\alpha_1}{dt} + C_2 \frac{d\alpha_2}{dt}$$
(12)

$$\sum_{i=1}^{N_C} C_i = 1 \tag{13}$$

Similarly, the overall activation energy is obtained by summing the individual activation energies corresponding to each reaction step, as expressed in Equation (14).

$$E_T = \sum_{i=1}^2 C_i E_i = C_1 E_1 + C_2 E_2 \tag{14}$$

The finite difference method was applied to numerically differentiate the conversion data, enabling the determination of the conversion rate derivative ($d\alpha/dT$), as shown in Equation (15).

$$\left(\frac{d\alpha}{dT}\right)_i = \frac{\alpha_{i+1} - \alpha_{i-1}}{T_{i+1} - T_{i-1}} \tag{15}$$

The DTG curve was obtained by computing the time derivative of the weight change at each point in the TGA data, as expressed in Equation (16).

$$\frac{dX_i}{dt} = \frac{X_{i+1} - X_i}{t_{i+1} - t_i} = \frac{X_{i+1} - X_i}{\Delta t}$$
 (16)

To obtain the optimal kinetic parameters, the nonlinear least-squares method was employed to minimize the objective function defined in Equation (17).

$$O.F. = \sum_{i=1}^{n_c} \left[\left(\frac{d \times}{dt} \right)_{exp,i} - \left(\frac{d \times}{dt} \right)_{calc,i} \right]^2$$
(17)

2.4.3. Kinetic Parameter Estimation via Non-Linear Optimization

A non-linear curve fitting approach was employed to estimate the pre-exponential factor (A) and activation energy (E) by minimizing the deviation between experimental TGA data and model predictions. The TGA model consists of a set of ordinary differential equations (ODEs), each describing the decomposition behavior of individual components [44]. MATLAB R2020a was used to implement a stochastic optimization technique, combining the "ga" (genetic algorithm) function with the "ode45" solver to optimize kinetic parameters. Due to the analytical complexity of Equation (10), numerical integration was required, with the fourth-order Runge-Kutta method applied to compute $g(\alpha)$ for given α values. The accuracy of the model fit was assessed using the correlation coefficient (R^2), calculated by comparing experimental and predicted data over all N measurement points (Equation (18)).

$$R^{2} = 1 - \frac{\sum_{i=1}^{N} (y_{exp,i} - y_{pred,i})^{2}}{\sum_{i=1}^{N} (y_{exp,i} - \bar{y}_{exp})^{2}}$$
(18)

In this equation, the subscripts "exp." and "pred." denote the experimental results and the predicted values obtained from theoretical integration, respectively. The variable N refers to the total number of experimental measurements considered. For the purpose of determining

the Mean Absolute Error (MAE), Mean Squared Error (MSE), and Mean Relative Error (MRE), equations (19)-(21) were utilized [45,46].

$$MAE = \frac{1}{N} \sum_{i=1}^{N} |y_{exp,i} - y_{pred,i}|$$
 (19)

$$MSE = \frac{1}{N} \sum_{i=1}^{N} (y_{exp,i} - y_{pred,i})^2$$
 (20)

$$MRE = \frac{1}{N} \sum_{i=1}^{N} \left| \frac{y_{exp,i} - y_{pred,i}}{y_{exp,i}} \right|$$
 (21)

Accordingly, the kinetic evaluation of coke decomposition was performed based on TGA data, using two independent parallel reactions. The overall decomposition process was represented by the following reaction model Equations (22)-(24).

$$\alpha = \alpha_1 + \alpha_2 \tag{22}$$

$$\frac{d\alpha_i}{dt} = \frac{A_i}{\beta} e^{-\frac{E_i}{RT}} f(\alpha_i)$$
 (23)

$$\frac{d^{\alpha}}{dt} = \frac{A_1}{\beta} e^{-\frac{E_1}{RT}} f(\alpha_1) + \frac{A_2}{\beta} e^{-\frac{E_2}{RT}} f(\alpha_2)$$
(24)

3. RESULTS AND DISCUSSION

3.1. X-Ray Diffraction Analysis

X-ray diffraction (XRD) analysis was conducted to determine the crystalline phases and structural characteristics of the synthesized zeolites, following established protocols [32]. The XRD patterns of Y- and Beta-zeolites are shown in Figures 3(a) and 3(b), respectively. For Yzeolite, four distinct low-angle reflections corresponding to the crystallographic planes [100], [110], [200], and [210] were observed, consistent with a hexagonal lattice and indicative of an ordered porous framework [3]. The intense [100] reflection at 20 of 5.87° confirms the long-range crystallinity of Y-zeolite. Similarly, Beta-zeolite exhibited its strongest reflection at 20 of 7.49°, attributed to the [100] plane. The positions and intensities of these peaks agree well with literature data [33] and standard patterns from the International Zeolite Association (IZA). Irregularities in peak shape, particularly in Beta-zeolite, are likely due to partial framework disorder and smaller crystallite size. According to Scherrer's equation, the full width at half maximum (FWHM) is inversely proportional to crystallite size. The broad peaks observed in the 2θ range of 2-40° for Beta-zeolite suggest a partially amorphous phase and a lower degree of crystallinity compared to Y-zeolite. In contrast, highly crystalline zeolites, such as Y-zeolite in this study, display sharp diffraction peaks with high intensity and a flat baseline [35].

3.2. Scanning Electron Microscope Analysis

Scanning electron microscopy (SEM) was employed to examine the morphology and crystallite size of Y- and Beta-zeolites at various magnifications [51]. As shown in **Figures 4** and **5**, both samples display uniformly distributed, rounded rectangular crystals and submicron-sized particle clusters, with no significant agglomeration observed. The crystallite sizes ranged from 0.35 to $0.5 \mu m$ for both zeolites, as illustrated in Figures 4 and 5 for Y- and Beta-zeolites, respectively. **Figures 4(b) and 5(b)** are the high magnification images of **Figures 4(b) and 5(b)**, respectively.

The observed particle sizes and morphological characteristics are consistent with literature values [37,38], confirming the typical crystal morphology and particle distribution for these zeolite types.

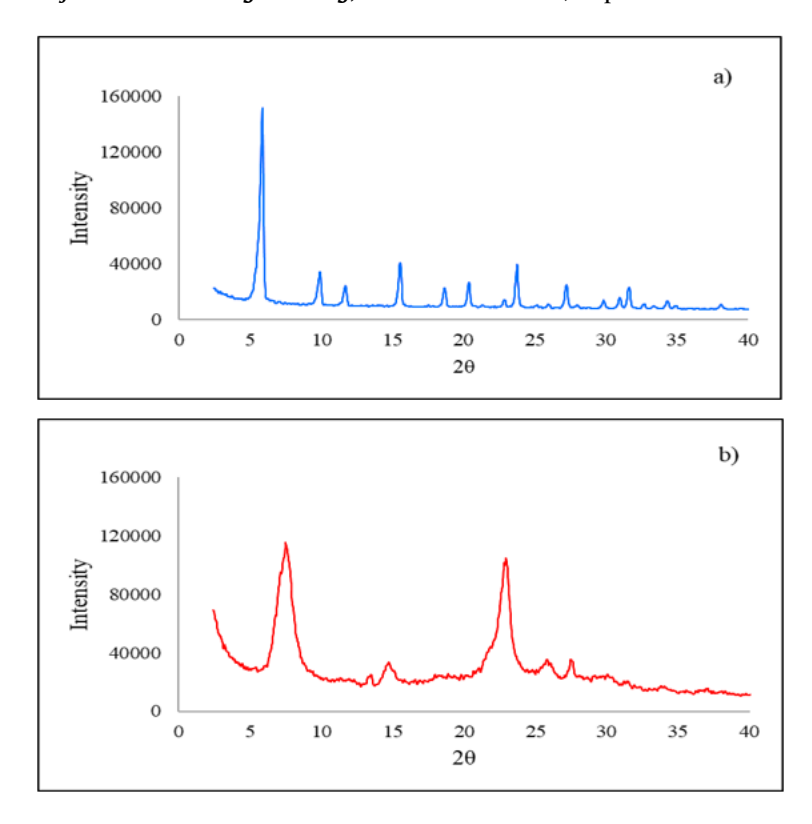


Figure 3. XRD patterns of (a) Y zeolite and (b) Beta zeolite.

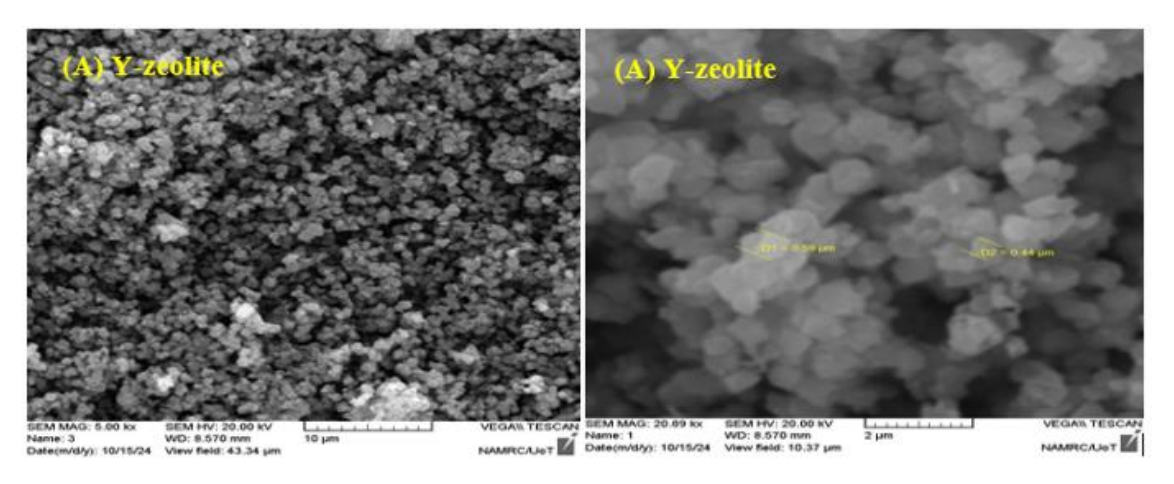


Figure 4. SEM-images of Y zeolite. Figure (b) is the high magnification image of Figure (1).

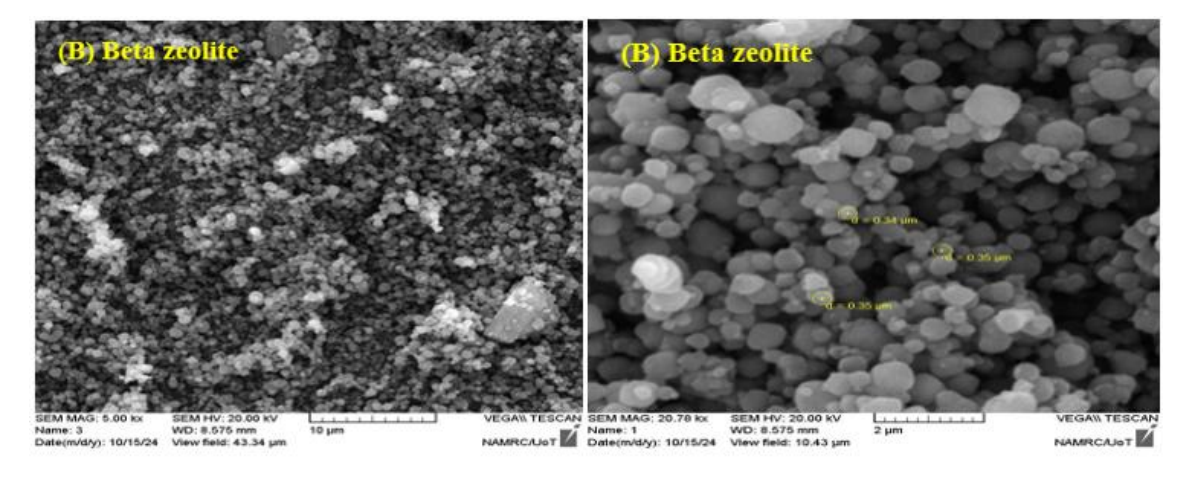


Figure 5. SEM-images of Beta zeolite. Figure (b) is the high magnification image of Figure (1)

3.3. Texture Property of Zeolite

The textural properties of the zeolite samples were evaluated using the BET method. As summarized in Table 1, the measured surface areas were 660 m²/g for Beta-zeolite and 875 m²/g for Y-zeolite. The higher surface area of Y-zeolite indicates an enhanced potential for reactant diffusion and adsorption due to its larger external pore volume, which is advantageous for catalytic performance, particularly in surface-controlled reactions such as heterogeneous catalysis [47]. The nitrogen adsorption—desorption isotherms, shown in Figure 6, exhibit a Type I profile, characteristic of microporous materials in both zeolites. This further underscores the suitability of Y-zeolite for catalytic processes such as alkylation, where higher external pore volume improves accessibility and available surface area. During such reactions, organic molecules of appropriate size are adsorbed into the external pores, where catalytic transformation occurs. The measured surface areas and isotherm behavior are consistent with literature values for similar zeolite materials [9,48,49], confirming the structural integrity and potential reactivity of the synthesized samples.

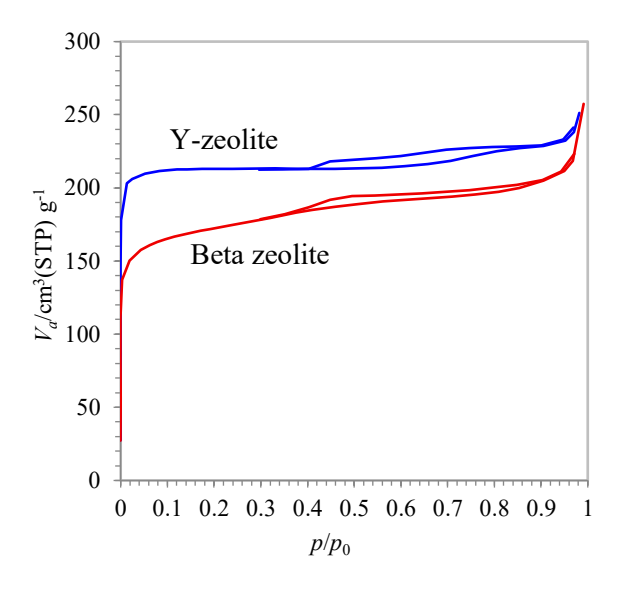


Figure 6. BET profiles and of Y-zeolite and Beta zeolite.

Table 1. Textural properties of zeolite catalysts.

Zeolite	* BET surface area (m²/g)	**Micropore Surface Area	**External Surface Area	*Total pore volume (m³/g)	**Micropore Volume	**External Pore Volume	*Average pore diameter (nm)
Beta zeolite	660	594	66	0.3950	0.2383	0.1567	1.77
Y-zeolite	875	861	14	0.3886	0.0656	0.3230	2.39

^{*} Brunauer-Emmett-Teller (BET) equation, **t-plot of Harkins-Jura equation.

3.4. Metal Content and Si/Al Ratio of Zeolites

The elemental composition of the zeolite catalysts was determined using X-ray fluorescence (XRF) and energy-dispersive X-ray spectroscopy (EDX) coupled with scanning electron microscopy (SEM). The Si/Al molar ratios of Y- and Beta-zeolites are presented in **Table 2**. The results from XRF and EDX analyses were in close agreement, with XRF providing slightly higher precision due to its bulk-sample analytical capability. The Si/Al ratio is a key parameter influencing zeolite acidity. Zeolites with a Si/Al ratio below 5 are generally classified as acidic catalysts, whereas those with higher ratios are more siliceous and less acidic. In this study, Y-zeolite exhibited a lower Si/Al ratio, indicating higher acidity, which is often associated with greater catalytic activity. In contrast, Beta-zeolite showed a significantly higher Si/Al ratio (exceeding 250), classifying it as a siliceous material with a lower density of acid sites. These findings are consistent with previously reported data for similar zeolite structures [50,51], confirming the reliability of the synthesis and characterization methods employed in this work.

Table 2. Si/Al molar ratio by XRF and EDX analyses of zeolite catalysts.

X-ray Instrument	Y-Zeolite	Beta Zeolite
Si/Al by XRF analysis	3.51 ± 0.1	293.93 ± 0.11
Si/Al by EDX analysis	2.6 ± 0.07	259.1 ± 0.14

3.5. Acidity of Zeolites

The acidity profiles of Y- and Beta-zeolites were evaluated using NH₃-temperature programmed desorption (NH₃-TPD), as shown in **Figure 7** and summarized in **Table 3**. The Alrich Y-zeolite exhibited significantly higher acidity compared to the Si-rich Beta-zeolite, with a total acid amount of 2.18 mmol/g, approximately 4.5 times greater than that of Beta-zeolite (0.48 mmol/g). In the weak acid region, Y-zeolite also demonstrated substantially higher acidity, with a measured value of 1.53 mmol/g, about 7.7 times higher than the 0.24 mmol/g observed for Beta-zeolite. Although Beta-zeolite displayed relatively low total acidity, the presence of 0.48 mmol/g of acid sites still indicates potential catalytic activity, particularly in reactions favoring mild acid strength. These results are consistent with the expected behavior based on the Si/Al ratio, where a lower ratio, as observed in Y-zeolite, typically correlates with higher acidity. The acidity distribution further explains the observed differences in catalytic performance between the two zeolite types.

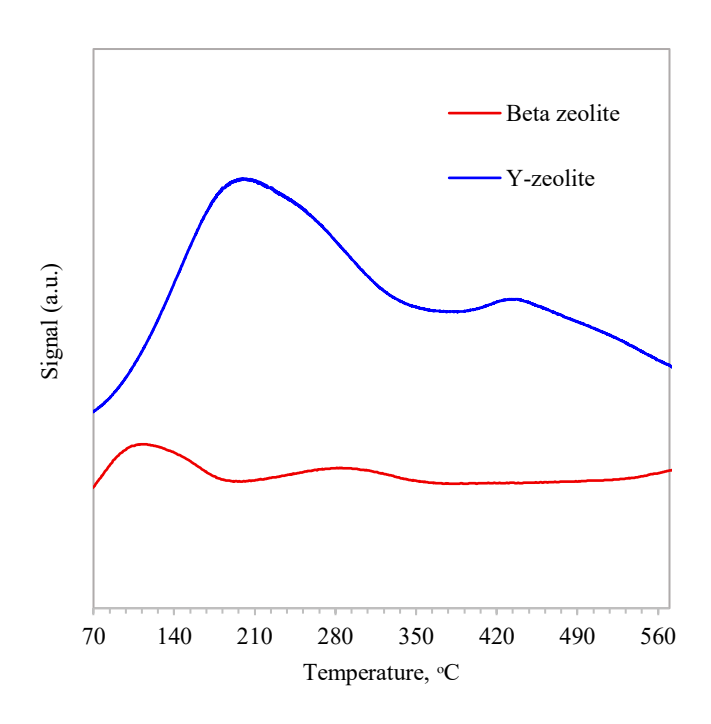


Figure 7. Zeolite acidity measured by NH3-TPD of Y-zeolite and Beta zeolite.

Table 3. Acidity of Y and Beta zeolites measured by NH3-TPD.

Catalyst	Weak acid amount, mmol/g	Strong acid amount, mmol/g	Total acid amount, mmol/g		
Y-zeolite	1.53	0.65	2.18		
Beta zeolite	0.24	0.20	0.48		

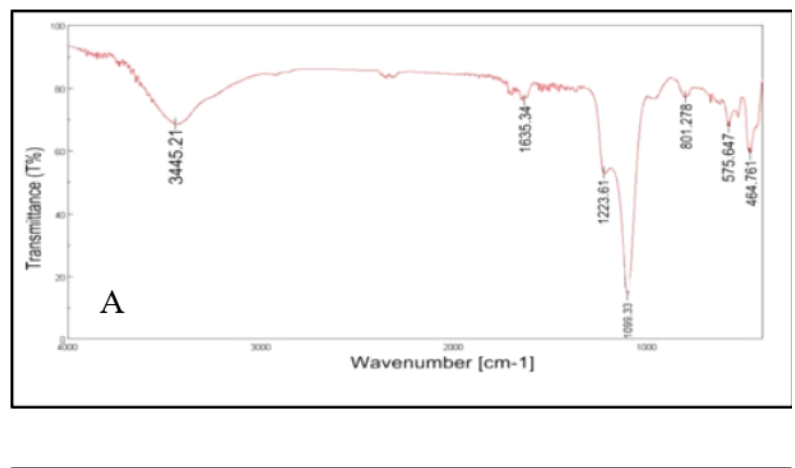
3.6. Fourier-Transform Infrared Spectroscopy Analysis

FTIR spectroscopy was employed to investigate the framework structure and surface functionalities of Y- and Beta-zeolites, with the spectra presented in Figures 8(a) and 8(b). Both materials exhibit characteristic vibrational bands corresponding to their tetrahedral framework and Si/Al composition. For Beta-zeolite, a strong and broad absorption band between 1099-1224 cm⁻¹ is assigned to asymmetric stretching vibrations of Si-O-Si and Si-O-Al bonds, indicative of high crystallinity and a high Si/Al ratio. Bands at 801 cm⁻¹ and 576 cm⁻¹ correspond to symmetric stretching and double-ring vibrations, respectively, characteristic of the Beta framework. A band at 465 cm⁻¹ is attributed to T-O bending vibrations (T = Si or Al). The presence of adsorbed water is confirmed by the H-O-H bending vibration at 1635 cm⁻¹, while a broad O-H stretching band near 3445 cm⁻¹ reflects surface hydroxyl groups. The relatively weaker and narrower O-H band suggests a more hydrophobic surface, consistent with the siliceous nature of Beta-zeolite, which favors nonpolar catalytic reactions [52]. In contrast, the FTIR spectrum of Y-zeolite displays framework bands in the 1052–1161 cm⁻¹ range, corresponding to asymmetric Si–O–Si and Si–O–Al stretching. A band at 669 cm⁻¹ is associated with external tetrahedral and double-ring (D6R) vibrations, characteristic of the Faujasite framework, while the 453 cm⁻¹ band confirms T–O bending. The O-H stretching band near 3430 cm⁻¹ is broader and more intense than in Beta-zeolite, indicating greater hydroxylation and a higher concentration of Brønsted acid sites, consistent with Y-zeolite's lower Si/Al ratio and stronger hydrophilic character. These spectral features confirm the structural integrity of both zeolites and highlight their contrasting surface properties and acidity profiles, which are critical for catalytic applications. The higher hydroxyl content and Al-rich composition of Y-zeolite favor acid-catalyzed and polar reactions, in agreement with previous studies [14,53-55], whereas the high-silica Beta-zeolite is better suited for hydrophobic and nonpolar processes.

3.7. Thermogravimetric Analysis of Coke Deposition over Zeolite

Thermogravimetric (TGA) and derivative thermogravimetric (DTG) analyses were employed to evaluate the structural stability and coke deposition behavior of Y- and Betazeolite catalysts following the alkylation reaction. Figures 9 and 10 present the thermal analysis profiles for beta zeolite and Y-zeolite, respectively, at heating rates of 5, 10, 15, and 20 °C/min. Figures 9(a) and 10(a) are the TG analysis results, and Figures 9(b) and 10(b) are the DTG results. The DTG curves for both catalysts display two distinct peaks. The first peak, appearing below 200 °C, corresponds to the desorption of physically adsorbed water and the removal of soft coke, a loosely bound carbonaceous deposit that blocks pores and restricts reactant diffusion. The second peak, observed between 200 and 350 °C, is attributed to the decomposition of hard coke, which strongly adheres to active sites and significantly deactivates the catalyst by covering acid sites through chemisorption. These observations are consistent with previous studies [14,56], which classify coke into two types: soft (or light) coke, formed at lower temperatures through condensation and molecular rearrangement, and hard (or heavy) coke, formed at higher temperatures (>350 °C), primarily via hydrogen transfer reactions on acidic sites, resulting in stable polyaromatic structures. Coke is widely

recognized as a secondary byproduct of hydrocarbon transformations, consisting of complex, non-volatile species with high boiling points. Consequently, total coke content represents a combination of soft precursors and more stable heavy coke deposits. The TG profiles exhibited minor variations with heating rate. As the heating rate increased, decomposition peaks shifted to higher temperatures by approximately 10 °C due to thermal gradients between the particle surface and core [41,57]. This behavior reflects the influence of heating rate on coke decomposition dynamics, which depend on coke type, quantity, catalyst structure, and acid site distribution [58]. Notably, the maximum decomposition rate was higher for Y-zeolite compared to Beta-zeolite, indicating greater coke accumulation. This is attributed to the higher acidity of Y-zeolite, associated with its lower Si/Al ratio, which promotes carbon buildup both on the surface and within the porous framework.



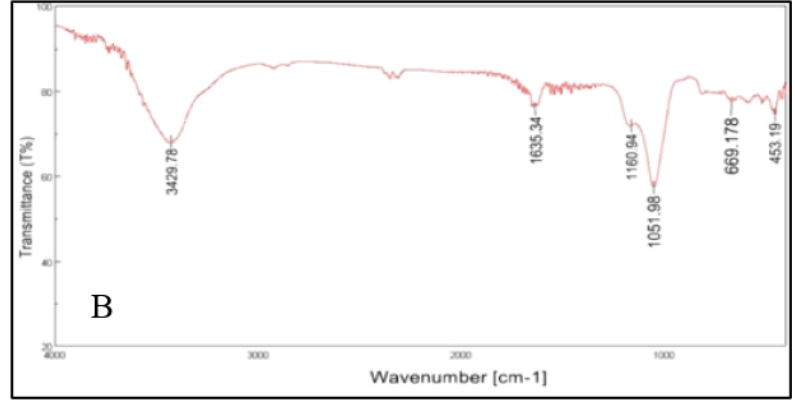


Figure 8. FTIR spectra results: (A) Beta zeolite and (B) Y-zeolite.

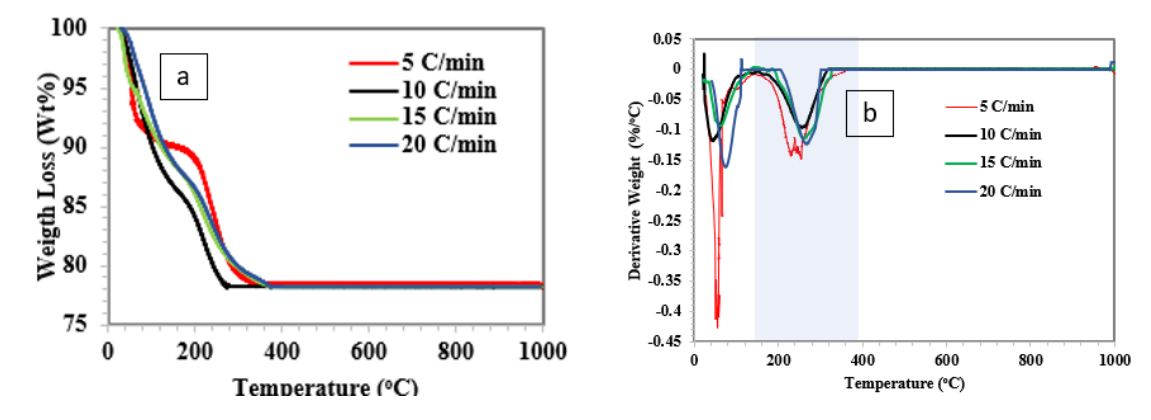
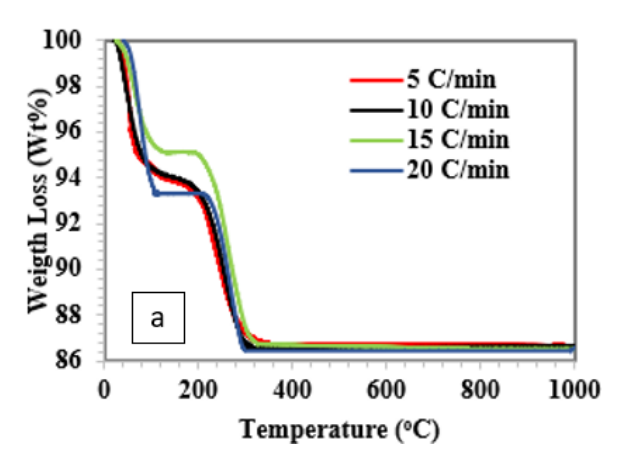


Figure 9. (a) TGA analysis of Beta zeolite, and (b) DTG analysis of Beta zeolite at different heating rates.



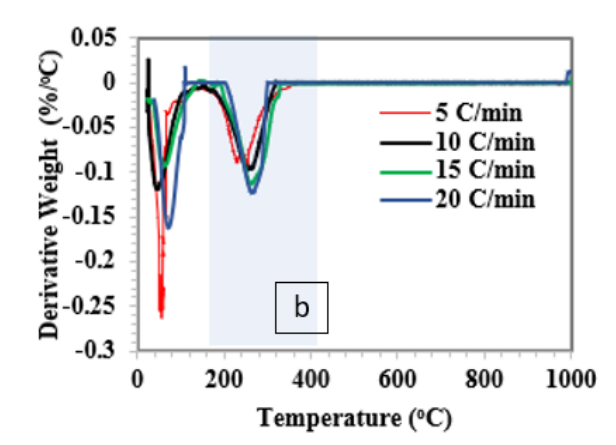


Figure 10. (a) TGA analysis of Y-zeolite, and (b) DTG analysis of Y-zeolite catalyst at different heating rates.

3.8. Catalytic Activity of Alkylation of Toluene

3.8.1. Effect of toluene/1-octene molar ratio

The influence of the toluene-to-1-octene molar ratio on olefin conversion and monoalkylation selectivity was investigated at 110 °C using an equal catalyst amount of 300 mg for both Y- and Beta-zeolites, as shown in **Figures 11(a)** and **11(b)**. Increasing the toluene-to-1-octene molar ratio from 3 to 9 significantly enhanced the conversion of 1-octene, from 31 to 87% for Y-zeolite and from 20 to 69% for Beta-zeolite. Furthermore, the selectivity toward 2-octyltoluene reached maximum values at a molar ratio of 9, measuring approximately 38% and 20% for Y- and Beta-zeolites, respectively. The elevated toluene-to-1-octene ratio facilitates the suppression of bulky byproducts, such as di- and trioctyltoluenes, thereby favoring the formation of mono-octyltoluenes via transalkylation reactions [14]. In addition, the selectivity toward monoalkylated products (2-, 3-, and 4-octyltoluenes) increased linearly for both catalysts, with 2-octyltoluene consistently remaining the dominant isomer. Accordingly, the optimal molar ratio was determined to be 9:1, which aligns well with previous studies [15].

3.8.2. Effect of reaction temperature

Reaction temperature has a significant impact on the alkylation of toluene with 1-octene. As shown in **Figures 12(a)** and **12(b)**, both the conversion of 1-octene and the selectivity toward mono-octyltoluene and other octyl isomers (2-, 3-, and 4-octyl toluene) were monitored over a range of temperatures using Y- and Beta-zeolite catalysts. In general, 1-octene conversion increased with rising temperature. For Y-zeolite, after 3 hours, the conversion reached approximately 61, 77, and 87% at 90, 100, and 110 °C, respectively. In contrast, Beta-zeolite exhibited lower conversions of about 17, 42, and 69% at the same temperatures. The highest selectivity for 2-octyltoluene was observed at 110 °C, with values of 38% for Y-zeolite and 20% for Beta-zeolite, whereas at 90 °C, the production of 2-octyltoluene was significantly lower. As conversion increased, the distribution of octyl isomers shifted, with the proportions of 2-, 3-, and 4-octyl toluene decreasing. For example, over Y-zeolite, the 2-octyl toluene fraction decreased from 24% at 90 °C to 9% at 110 °C, while over Beta-zeolite, it declined from 20 to 16%. This behavior is likely due to enhanced diffusion of reactants into the bulkier mono-octyltoluene products at higher temperatures, combined with faster isomerization of 1-octene toward equilibrium.

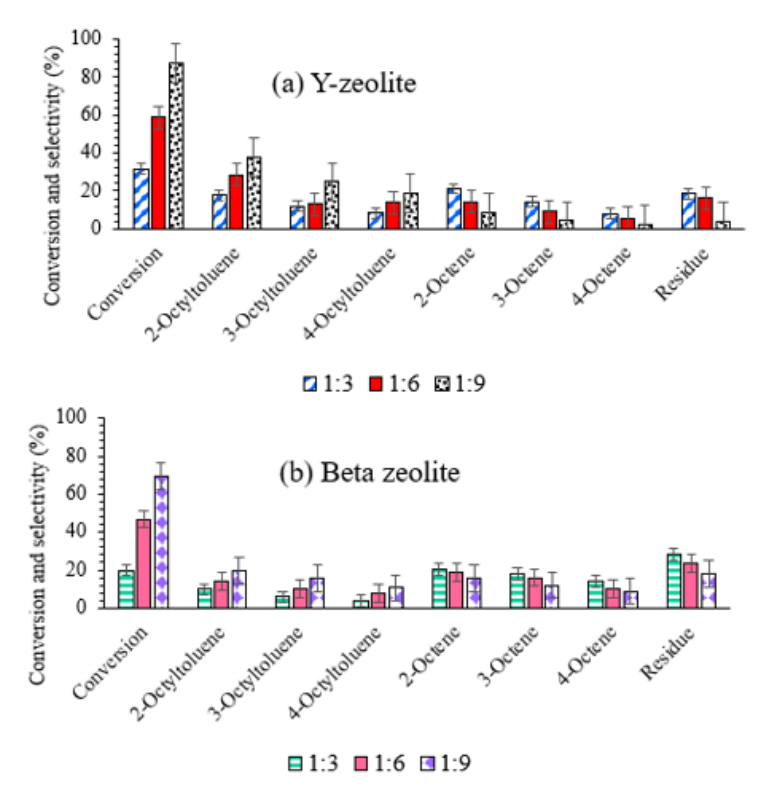
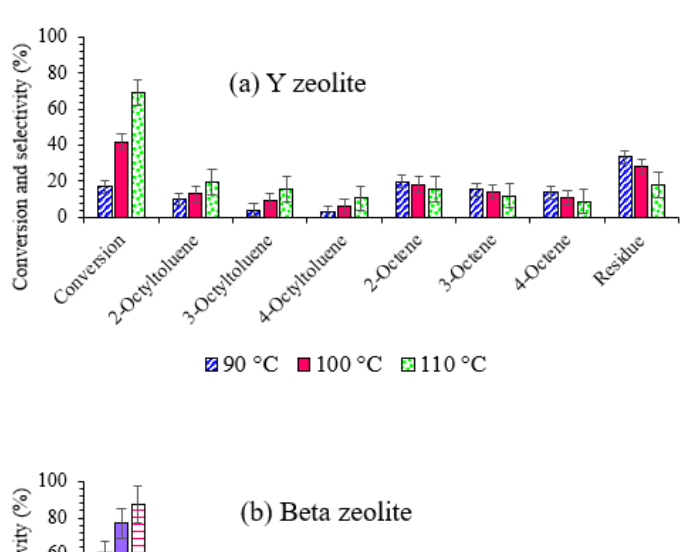


Figure 11. (a) Y-zeolite and (b) Beta zeolite catalysts at 110 °C.



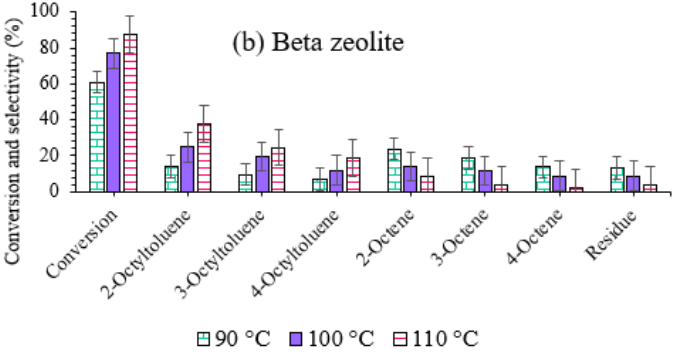
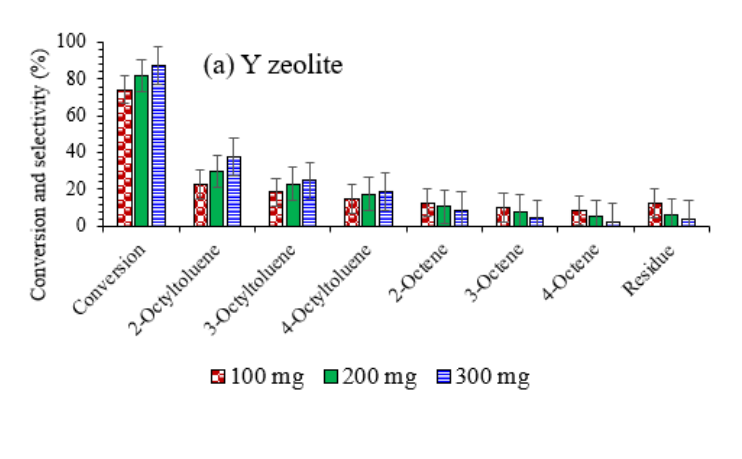


Figure 12. (a) Beta zeolite and (b) Y-zeolite catalysts at toluene-to-1-octene molar ratio 9:1.

3.8.3. Effect of catalyst loading on 1-octene conversion and selectivity

The effect of catalyst loading and the contrasting acidity of Al-rich Y-zeolite and Si-rich Beta-zeolite on 1-octene conversion was investigated by varying the catalyst amount from

100 to 300 mg. As shown in Figures 13(a) and 13(b), conversion increased with catalyst loading, reaching a maximum at 300 mg for both catalysts. This enhancement is attributed to the higher number of accessible acid sites and increased surface area (Tables 1 and 3), particularly for Y-zeolite, which facilitates carbenium ion formation and thus accelerates the alkylation reaction [14]. Under these conditions, 1-octene conversion using Y-zeolite reached approximately 78, 82, and 88% at 100, 200, and 300 mg, respectively. In comparison, Betazeolite exhibited lower conversions of 45, 61, and 69% under identical conditions, reflecting its higher Si/Al ratio and lower acidity. Catalyst loading also influenced the selectivity toward monoalkyltoluene isomers. For Y-zeolite (Figure 13(a)), the selectivity of 2-octyltoluene increased from 24 to 38%, 3-octyltoluene from 18 to 24%, and 4-octyltoluene from 17 to 22% with increasing catalyst amount. Similar trends were observed for Beta-zeolite (Figure 13(b)), although at lower selectivity levels: 2-octyltoluene increased from 11 to 19%, 3-octyltoluene from 7 to 16%, and 4-octyltoluene from 5 to 11%. At a reaction temperature of 110 °C and a toluene-to-1-octene molar ratio of 9:1, product distribution favored the formation of the 2octyltoluene isomer for both catalysts. This preference is particularly pronounced for Betazeolite, whose lower external pore volume (Table 1) restricts the formation of bulkier alkylated products within internal channels, thereby promoting reactions primarily on the external surface [59].



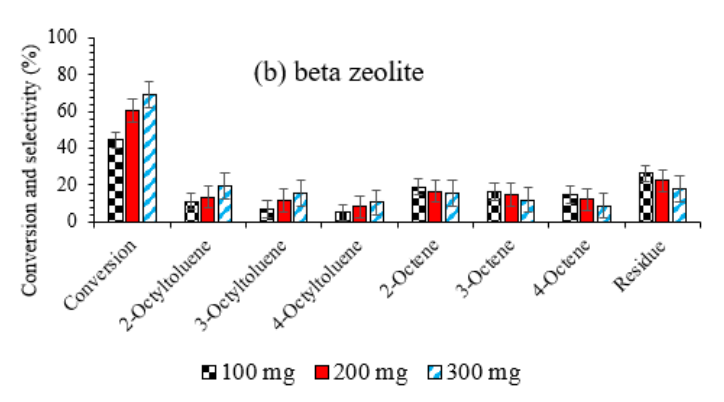


Figure 13. (a) Y-zeolite, and (b) Beta zeolite catalysts at 110 °C and toluene-to-1-octene molar ratio 9:1.

3.8.4. Effect of time on stream study of catalytic performance

Figure 14 illustrates the effect of time on stream (TOS) on the catalytic performance of Y-and Beta-zeolites. The reactions were conducted at 110 °C with a toluene-to-1-octene molar ratio of 9:1 and a catalyst loading of 300 mg, conditions under which both catalysts achieved relatively high conversions. For Y-zeolite, the conversion of 1-octene increased from

approximately 65% at 30 minutes to around 90% at 180 minutes. Notably, after 120 minutes, the conversion reached a plateau, rising only slightly from 87% at 120 minutes to 90% at 180 minutes, indicating that the reaction likely approached a steady state beyond the 2-hour mark. In contrast, Beta-zeolite exhibited a more gradual conversion profile, starting at 33% after 30 minutes and reaching 70% at 180 minutes. Overall, Al-rich Y-zeolite demonstrated superior catalytic performance compared to Si-rich Beta-zeolite, achieving nearly 20% higher conversion after 180 minutes. This enhanced activity is likely due to Y-zeolite's lower Si/Al ratio, which provides a higher density of acid sites, facilitating carbenium ion formation and promoting the alkylation reaction more effectively.

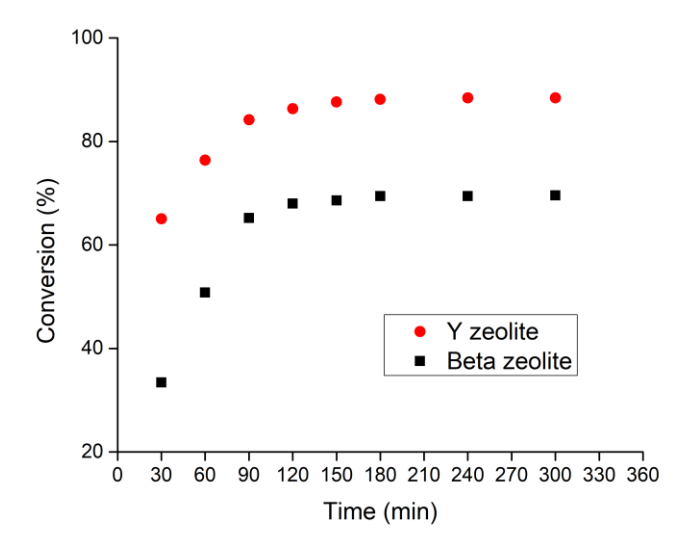


Figure 14. Effect of TOS of alkylation reaction at 110 °C and toluene-to-1-octene molar ratio 9:1.

3.9. Effect of TGA Kinetics

The pre-exponential factors (Arrhenius constants) and the corresponding decoking activation energies of the two zeolites were determined through computational optimization of kinetic parameters to fit the experimental TGA data for coke-deactivated Beta- and Y-zeolite catalysts at various heating rates (**Figures 9 and 10**). The simulated TGA results are summarized in **Table 4**. Kinetic evaluation based on reaction model calculations yielded high correlation coefficients ($R^2 \approx 0.995$) for both catalysts, indicating excellent agreement with experimental data. For Beta-zeolite, the decoking activation energies were 29.21 and 65.07 kJ/mol for soft and hard coke, respectively. For Y-zeolite, the corresponding activation energies were 37.20 and 67.41 kJ/mol for soft and hard coke, respectively. The increase in hard coke content, consisting mainly of amorphous carbon, led to higher activation energies for its decomposition. Since the spent zeolites contain a mixture of coke types, the decoking process proceeds via two primary reactions, corresponding to the pyrolysis of soft and hard coke at different temperature ranges. The determined decomposition activation energies (Ea), pre-exponential factors (A_0), and weight fractions of carbonaceous deposits for both coke types were in reasonable agreement with values reported in the literature [14,60].

Figures 15 and 16 present a comparison between the experimental and simulated TGA curves for Beta- and Y-zeolite catalysts deactivated by coke, respectively. TGA measurements were conducted at four heating rates: 5, 10, 15, and 20 °C/min. The correlation coefficients for all eight curves were consistently high, indicating that the multi-curve kinetic model

accurately captures the decomposition behavior of both Beta and Y zeolites. Overall, a strong agreement is observed between the developed reaction model and the experimental data, particularly within the two-step reaction framework. In this model, α_1 and α_2 represent the degrees of conversion associated with the removal of soft coke and hard coke, respectively.

Table 4. Kinetic parameters of the catalyst decoking process of two zeolites.

Catalyst	Soft Coke	Hard Coke	Soft Coke	Hard Coke	Soft Coke	Hard Coke	
	Ao	Ao	Еа	Еа	% Weight	% Weight	R^2
			(kJ/mol)	(kJ/mol)	fraction	fraction	
Beta zeolite	32889.054	1172392.81	29.213	65.073	0.447	0.549	0.995
Y-zeolite	63259.456	2162227.39	37.196	67.411	0.451	0.553	0.996

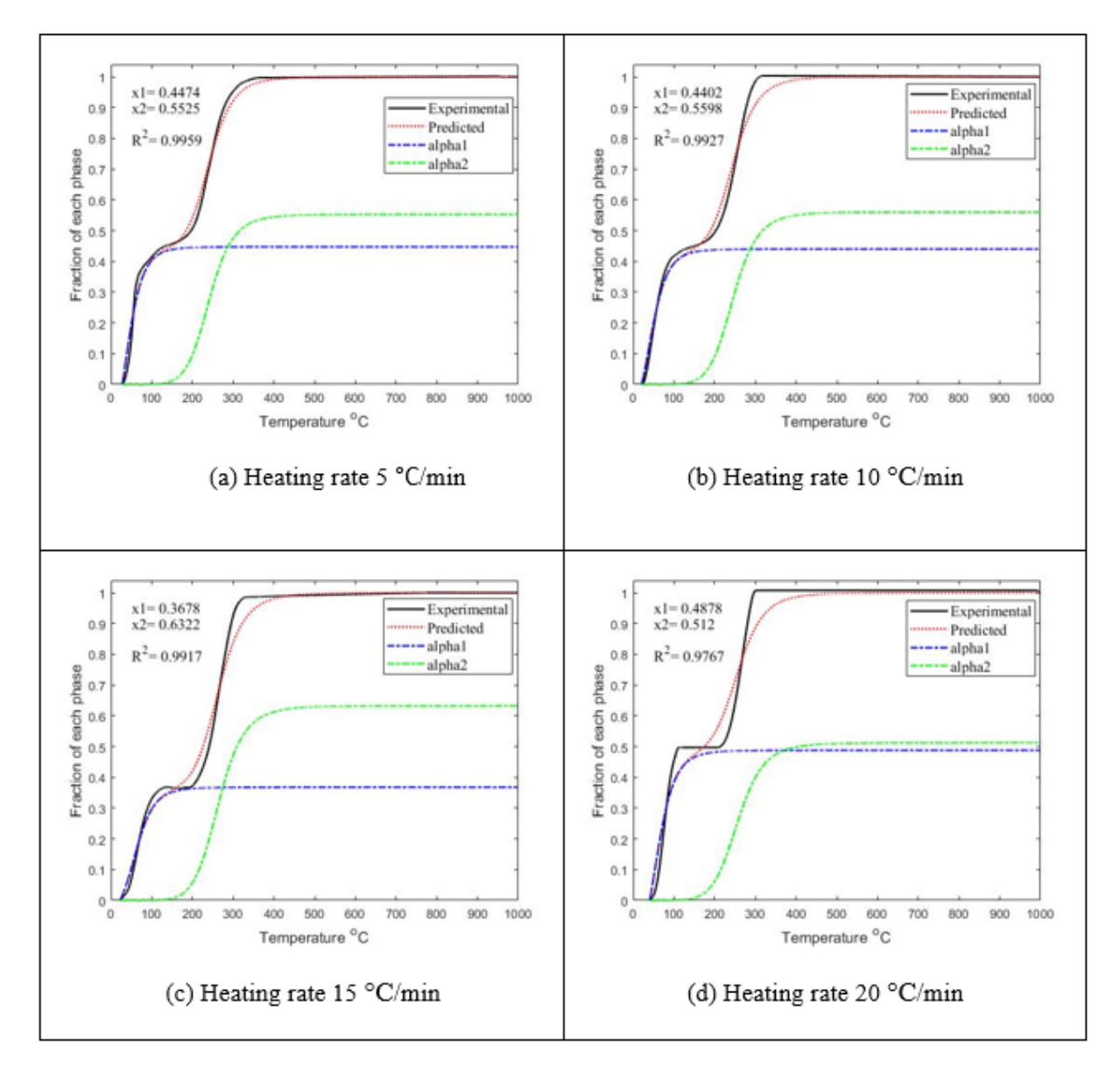


Figure 15. Comparison of experimental and predicted TGA for Beta zeolite catalyst at different TGA heating rates: (a) 5, (b) 10, (c) 15, and (d) 20 °C/min.

The TGA simulation results indicate that the decomposition of soft coke (blue curve) occurs at temperatures between 100 and 200 °C, while hard coke (green curve) decomposes at higher temperatures, from 200 to 350 °C. The amount of soft coke accumulated on both

catalysts is lower than that of hard coke. Notably, the fractions of soft and hard coke deposited on Y-zeolite (0.451 and 0.553 wt%, respectively) are slightly higher than those on Beta-zeolite (0.447 and 0.549 wt%). This observation is consistent with the physical properties of Y-zeolite, which possesses higher acidity, larger surface area, and greater pore volume, facilitating increased coke deposition. As presented in **Table 4**, the activation energy for the second reaction step, corresponding to hard coke removal, is higher for both catalysts, indicating that hard coke is more strongly bound to the zeolite surface, likely via chemical interactions with the catalyst framework, and thus requires more energy for decomposition. In contrast, soft coke, being primarily physically adsorbed, is removed more easily at lower temperatures. Overall, the activation energies for coke decomposition on Beta-zeolite are generally lower than those on Y-zeolite, reflecting that Beta requires less energy for coke removal. This difference is attributed to the higher catalytic activity of Y-zeolite during the alkylation reaction, which promotes greater coke formation and higher pre-exponential factors, corresponding to an increased frequency of molecular collisions during decomposition. These findings are in agreement with previously reported literature [61].

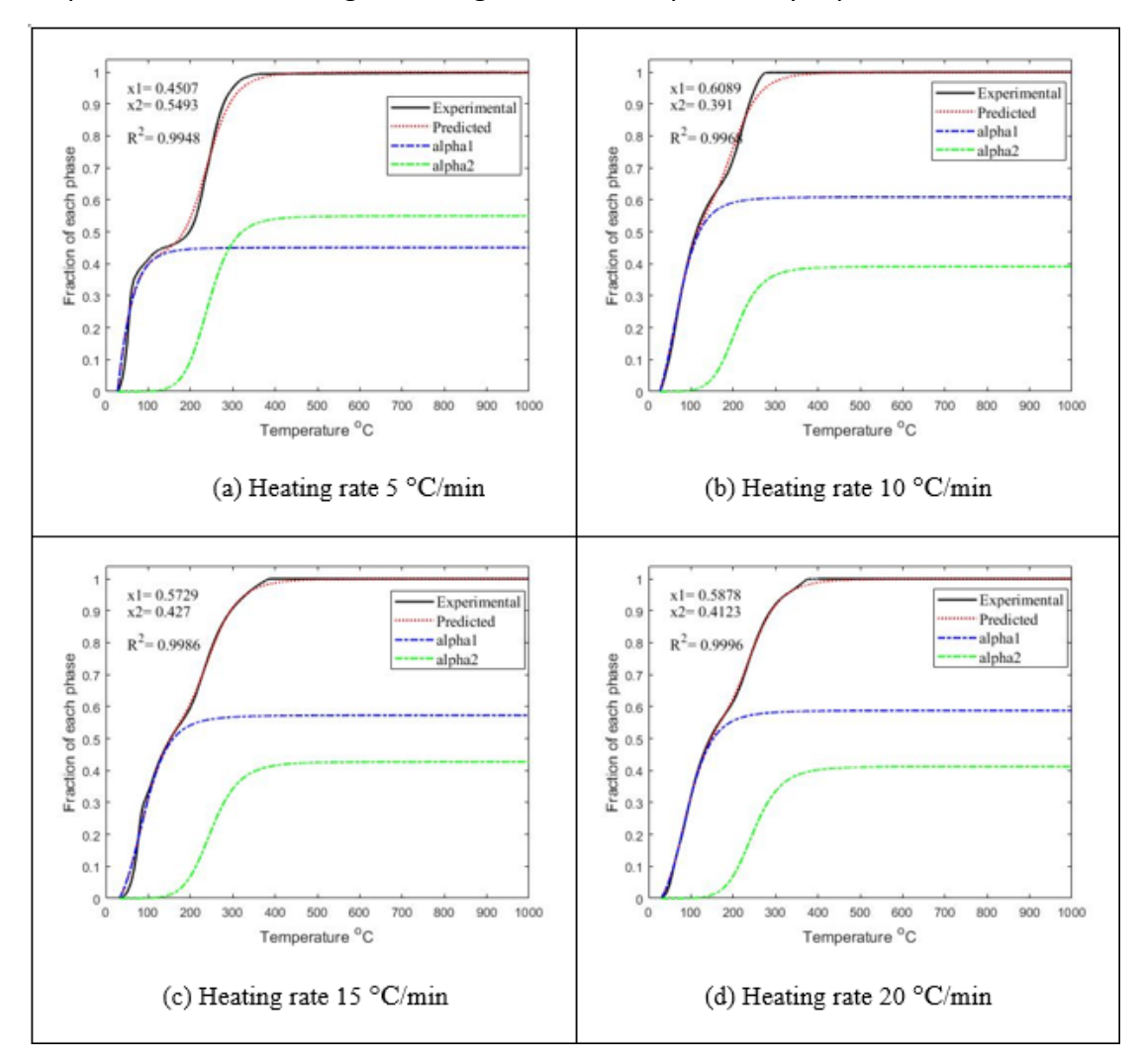


Figure 16. Comparison between the experimental and the predicted data for Y zeolite catalyst at different TGA heating rates: (a) 5, (b) 10, (c) 15, and (d) 20 °C/min.

4. CONCLUSION

In this study, the catalytic performance of Al-rich Y-zeolite and Si-rich Beta zeolite was systematically evaluated for the liquid-phase alkylation of toluene with 1-octene under varying reaction conditions, including reaction temperature, feed ratios, and catalyst loading, to assess their impact on conversion and product selectivity. Reaction temperature significantly influenced both 1-octene conversion and monoalkyltoluene selectivity, which can be attributed to enhanced diffusivity and accelerated olefin isomerization at elevated temperatures. Increasing catalyst loading improved conversion for both zeolites, with Yzeolite consistently showing higher selectivity across all isomers due to its greater density of acid sites, resulting from a lower Si/Al ratio and larger external pore volume. Time-on-stream studies demonstrated steady-state behaviour, suggesting that the higher acidity and superior pore structure of Y-zeolite facilitated more efficient formation of carbenium ions required for alkylation. Thermogravimetric analysis (TGA/DTG) revealed two distinct coke decomposition peaks corresponding to soft and hard coke, reflecting catalyst deactivation patterns. The activation energies for coke removal were slightly lower for Beta-zeolite (29.2 and 65.1 kJ/mol for soft and hard coke) compared to Y-zeolite (37.2 and 67.4 kJ/mol), indicating that coke deposited on Beta is less strongly bound. Nevertheless, Y-zeolite accumulated slightly more coke, consistent with its higher catalytic activity and acid site density. In summary, Al-rich Yzeolite exhibited superior catalytic performance in terms of conversion, selectivity, and reaction stability, attributed to its higher acidity, larger external pore volume, and favorable pore architecture. These results emphasize the critical role of catalyst composition and structural features in optimizing the alkylation of toluene with long-chain olefins.

5. ACKNOWLEDGMENT

The authors gratefully acknowledge the support of University Mohammed Premier, Oujda, Morocco, and the Laboratory of the Higher Institute of Nursing and Health Techniques (ISPITS), Oujda, Morocco. Special thanks are extended to the Project CNRST / TUBITAK (2023–2025), a collaborative initiative between University Mohammed Premier, Morocco and Inonu University, Turkey, for their valuable financial and institutional support throughout the course of this research.

6. AUTHORS' NOTE

The authors are grateful to the Chemical Engineering Collage, University of Technology-Iraq, Baghdad, Iraq for providing space and facilities to conduct this work.

7. REFERENCES

- [1] Kuvayskaya, A., Mohseni, R., and Vasiliev, A. (2022). Alkylation of benzene by long-chain alkenes on immobilized phosphotungstic acid. *Journal of Porous Materials*, 29(3), 705-711.
- [2] Misaki, S., Takabatake, M., Hasegawa, S., Manaka, Y., Chun, W. J., and Motokura, K. (2024). Effect of zeolites on the alkylation of aromatics with alkanes using a Pd nanoparticle/solid acid cooperative catalytic system. *Green Carbon*, 2(3), 282-290.
- [3] Kim, H. S., Lee, H., Park, H., Song, I., and Kim, D. H. (2024). Revealing the two distinctive roles of HY zeolite in enhancing the activity and durability of manganese oxide-zeolite hybrid catalysts for low-temperature NH3-SCR. *Applied Catalysis B: Environment and Energy*, 355, 124199.

- [4] Pan, A., Chojnacka, M., Crowley, R., Göttemann, L., Haines, B. E., and Kou, K. G. (2022). Synergistic Brønsted/Lewis acid catalyzed aromatic alkylation with unactivated tertiary alcohols or di-tert-butylperoxide to synthesize quaternary carbon centers. *Chemical Science*, *13*(12), 3539-3548.
- [5] Lee, D. W., and Yoo, B. R. (2014). Advanced metal oxide (supported) catalysts: Synthesis and applications. *Journal of Industrial and Engineering Chemistry*, 20(6), 3947-3959.
- [6] Sohn, S., and Do, P. (2023). Linear alkylbenzenes: An overview of the commercial hf and detal[™] process unit alkylation technology (case study). *Industrial Arene Chemistry: Markets, Technologies, Sustainable Processes and Cases Studies of Aromatic Commodities*, 2, 729-745.
- [7] Miceli, M., Frontera, P., Macario, A., and Malara, A. (2021). Recovery/reuse of heterogeneous supported spent catalysts. *Catalysts*, *11*(5), 591.
- [8] Al-Sultani, S. H., Al-Shathr, A., and Al-Zaidi, B. Y. (2024). Aromatics alkylated with olefins utilizing zeolites as heterogeneous catalysts: A review. *Reactions*, *5*(4), 900-927.
- [9] Al-Zaidi, B. Y., Al-Shathr, A., Shehab, A. K., Shakor, Z. M., Majdi, H. S., AbdulRazak, A. A., and McGregor, J. (2023). Hydroisomerisation and hydrocracking of n-heptane: modelling and optimisation using a hybrid artificial neural network–genetic algorithm (ANN–GA). *Catalysts*, *13*(7), 1125.
- [10] Ali, N. S., Salih, I. K., Harharah, H. N., Majdi, H. S., Salih, H. G., Kalash, K. R., and Zendehboudi, S. (2023). Utilization of loaded cobalt onto MCM-48 mesoporous catalyst as a heterogeneous reaction in a fixed bed membrane reactor to produce isomerization product from n-heptane. *Catalysts*, *13*(7), 1138.
- [11] Khalil, M., Al-Zaidi, B. Y., Shakor, Z. M., Hussein, S. J., and Al-Shathr, A. (2023). experimental and kinetic study of the catalytic behavior of sulfate-treated nanostructured bifunctional zirconium oxide catalysts in n-heptane hydroisomerization reactions. *ChemEngineering*, 7(6), 115.
- [12] Kadja, G. T., Azhari, N. J., Mardiana, S., Culsum, N. T., and Maghfirah, A. (2023). Recent advances in the development of nanosheet zeolites as heterogeneous catalysts. *Results in Engineering*, *17*, 100910.
- [13] Liang, J., Liang, Z., Zou, R., and Zhao, Y. (2017). Heterogeneous catalysis in zeolites, mesoporous silica, and metal—organic frameworks. *Advanced Materials*, 29(30), 1701139.
- [14] Al-Sultani, S. H., Al-Shathr, A., and Al-Zaidi, B. Y. (2024). Toluene alkylation reactions over y-type zeolite catalysts: an experimental and kinetic study. *Reactions*, *5*(4), 2624-781X.
- [15] Liu, Y., Xu, L., Xu, B., Li, Z., Jia, L., and Guo, W. (2009). Toluene alkylation with 1-octene over supported heteropoly acids on MCM-41 catalysts. *Journal of Molecular Catalysis A: Chemical*, 297(2), 86-92.
- [16] Borutskii, P. N., Kozlova, E. G., Podkletnova, N. M., Gil'Chenok, N. D., Sokolov, B. G., Zuev, V. A., and Shatovkin, A. A. (2007). Alkylation of benzene with higher olefins on heterogeneous catalysts. *Petroleum Chemistry*, 47(4), 250-261.
- [17] Armor, J. N. (2011). A history of industrial catalysis. Catalysis Today, 163(1), 3-9.
- [18] Degnan Jr, T. F., Smith, C. M., and Venkat, C. R. (2001). Alkylation of aromatics with ethylene and propylene: recent developments in commercial processes. *Applied catalysis A: general*, 221(1-2), 283-294.
- [19] Weitkamp, J. (2000). Zeolites and catalysis. Solid State Ionics, 131(1-2), 175-188.
- [20] Shamzhy, M., Opanasenko, M., Concepción, P., and Martínez, A. (2019). New trends in tailoring active sites in zeolite-based catalysts. *Chemical Society Reviews*, 48(4), 1095-1149.

- [21] Lin, M., Zhou, S., Zhang, C., Li, Y., Wang, C., and Shu, X. (2022). An efficient preparation method of Y zeolite-based catalyst for Isobutane-butene alkylation. *Fuel*, *328*, 125371.
- [22] Da, Z., Han, Z., Magnoux, P., and Guisnet, M. (2001). Liquid-phase alkylation of toluene with long-chain alkenes over HFAU and HBEA zeolites. *Applied Catalysis A: General*, 219(1-2), 45-52.
- [23] Shakor, Z. M., and Al-Shafei, E. N. (2023). The mathematical catalyst deactivation models: a mini review. *RSC Advances*, *13*(32), 22579-22592.
- [24] Devaraj, A., Vijayakumar, M., Bao, J., Guo, M. F., Derewinski, M. A., Xu, Z., and Ramasamy, K. K. (2016). Discerning the location and nature of coke deposition from surface to bulk of spent zeolite catalysts. *Scientific Reports*, 6(1), 37586.
- [25] Al-Shathr, A., Al-Zaidi, B. Y., Shehab, A. K., Shakoor, Z. M., Aal-Kaeb, S., Gomez, L. Q., and McGregor, J. (2023). Experimental and kinetic studies of the advantages of coke accumulation over Beta and Mordenite catalysts according to the pore mouth catalysis hypothesis. *Catalysis Communications*, 181, 106718.
- [26] Mayerová, J., Pawlesa, J., Košová, G., and Čejka, J. (2005). Microporous and mesoporous molecular sieves for alkylation of toluene with olefins. In *Studies in Surface Science and Catalysis*, *158*, 1945-1952.
- [27] Fernandes, R. M., and Lachter, E. R. (2005). Evaluation of sulfonic resins for liquid phase alkylation of toluene. *Catalysis Communications*, 6(8), 550-554.
- [28] Ogunbadejo, B., Aitani, A., Čejka, J., Kubů, M., and Al-Khattaf, S. (2016). The effect of alkylation route on ethyltoluene production over different structural types of zeolites. *Chemical Engineering Journal*, *306*, 1071-1080.
- [29] Zhou, F., Gao, Y., Wu, G., Ma, F., and Liu, C. (2017). Improved catalytic performance and decreased coke formation in post-treated ZSM-5 zeolites for methanol aromatization. *Microporous and Mesoporous Materials*, *240*, 96-107.
- [30] Guisnet, M., and Magnoux, P. (1989). Coking and deactivation of zeolites: influence of the pore structure. *Applied Catalysis*, *54*(1), 1-27.
- [31] Brillis, A. A., and Manos, G. (2003). Coke formation during catalytic cracking of C8 aliphatic hydrocarbons over ultrastable Y zeolite. *Industrial & Engineering Chemistry Research*, 42(11), 2292-2298.
- [32] Quintana-Gómez, L., Connolly, M., Shehab, A. K., Al-Shathr, A., and McGregor, J. (2022). "Reverse combustion" of carbon dioxide in water: The influence of reaction conditions. *Frontiers in Energy Research*, *10*, 917943.
- [33] Liang, B., Liu, M. N., An, N., Ren, F., Luo, Q. X., Chen, H., and Hao, Q. Q. (2024). Achieving long-lived MWW zeolite catalyst for alkylation of benzene with 1-dodecene: Insights into confinement effect of surface cavities and underlying mechanism. *Chemical Engineering Journal*, 489, 151109.
- [34] Shen, H., Liu, M., Li, J., Li, X., Xie, S., Chen, F., AND Zhu, X. (2021). Promising strategy to synthesize ZSM-5@ Silicalite-1 with superior catalytic performance for catalytic cracking reactions. *Industrial & Engineering Chemistry Research*, 60(25), 9098-9106.
- [35] Ghanbari-Siahkali, A., Philippou, A., Dwyer, J., and Anderson, M. W. (2000). The acidity and catalytic activity of heteropoly acid on MCM-41 investigated by MAS NMR, FTIR and catalytic tests. *Applied Catalysis A: General*, 192(1), 57-69.
- [36] Golding, C. G., Lamboo, L. L., Beniac, D. R., and Booth, T. F. (2016). The scanning electron microscope in microbiology and diagnosis of infectious disease. *Scientific Reports*, 6(1), 26516.
- [37] Sombatchaisak, S., Praserthdam, P., Chaisuk, C., AND Panpranot, J. (2004). An alternative correlation equation between particle size and structure stability of H– Y

- zeolite under hydrothermal treatment conditions. *Industrial & Engineering Chemistry Research*, 43(15), 4066-4072.
- [38] Tianying, N. I. U., Yingxia, L. I., Jianwei, L. I., and Biaohua, C. H. E. N. (2009). Synthesis of zeolite beta by the vapour-phase transport method using tetraethylammonium bromide as the organic template. *Chinese Journal of Catalysis*, 30(3), 191-195.
- [39] Shakor, Z., Alasseel, A., and Al-Shafei, E. (2024). The structure of deposited coke on hydrocracking and reforming catalysts: Coke deactivation and kinetics. *The Canadian Journal of Chemical Engineering*, 102(8), 2876-2891.
- [40] Al-Karim, A. A., Shakor, Z. M., Al-Sheikh, F., and Anderson, W. A. (2022). Experimental and kinetic study of vacuum residue cracking over zirconium based catalysts. *Reaction Kinetics, Mechanisms and Catalysis*, 135(2), 847-865.
- [41] Hussein, Z. A., Shakor, Z. M., Alzuhairi, M., and Al-Sheikh, F. (2023). Thermal and catalytic cracking of plastic waste: a review. *International Journal of Environmental Analytical Chemistry*, 103(17), 5920-5937.
- [42] Hussein, Z. A., Shakor, Z. M., Alzuhairi, M., and Al-Sheikh, F. (2023). Kinetic and thermodynamic study of the pyrolysis of plastic waste. *Environmental Processes*, 10(2), 27.
- [43] Biney, P. O., Gyamerah, M., Shen, J., and Menezes, B. (2015). Kinetics of the pyrolysis of arundo, sawdust, corn stover and switch grass biomass by thermogravimetric analysis using a multi-stage model. *Bioresource Technology*, 179, 113-122.
- [44] Burra, K. R. G., and Gupta, A. K. (2019). Modeling of biomass pyrolysis kinetics using sequential multi-step reaction model. *Fuel*, *237*, 1057-1067.
- [45] Al-Shathr, A., Shakor, Z. M., Al-Zaidi, B. Y., Majdi, H. S., AbdulRazak, A. A., Aal-Kaeb, S., and McGregor, J. (2022). Reaction kinetics of cinnamaldehyde hydrogenation over Pt/SiO2: comparison between bulk and intraparticle diffusion models. *International Journal of Chemical Engineering*, 2022(1), 8303874.
- [46] Al-Shathr, A., Shakor, Z. M., Majdi, H. S., AbdulRazak, A. A., and Albayati, T. M. (2021). Comparison between artificial neural network and rigorous mathematical model in simulation of industrial heavy naphtha reforming process. *Catalysts*, *11*(9), 1034.
- [47] AlKhafaji, K. S., Shakor, Z. M., Al-Zaidi, B. Y., and Hussein, S. J. (2022). Preparation and characterization of metakaolin-based catalysts for gasoil hydrodesulfurization purposes. *Arabian Journal for Science and Engineering*, *47*(5), 6283-6296.
- [48] Da, Z., Magnoux, P., and Guisnet, M. (1999). Liquid phase alkylation of toluene with 1-heptene over a HFAU zeolite: evidence for transalkylation between toluene and non-desorbed products. Applied Catalysis A: General, 182(2), 407-411.
- [49] Pérez-Botella, E., Valencia, S., and Rey, F. (2022). Zeolites in adsorption processes: State of the art and future prospects. *Chemical Reviews*, 122(24), 17647-17695.
- [50] Wei, L., Yang, H., Ren, P., Yang, Y., Li, Y. W., Li, R., and Jiao, H. (2022). Distribution of multiple Al substitution in HY zeolite and Brønsted acid strength-A periodic DFT study. *Microporous and Mesoporous Materials*, *344*, 112184.
- [51] Xiong, G., Feng, M., Liu, J., Meng, Q., Liu, L., and Guo, H. (2019). The synthesis of hierarchical high-silica beta zeolites in NaF media. *RSC Advances*, *9*(7), 3653-3660.
- [52] Khaleque, A., Alam, M. M., Hoque, M., Mondal, S., Haider, J. B., Xu, B., and Moni, M. A. (2020). Zeolite synthesis from low-cost materials and environmental applications: A review. *Environmental Advances*, 2, 100019.
- [53] Corma, A., Martinez, A., Martinezsoria, V., and Monton, J. B. (1995). Hydrocracking of vacuum gasoil on the novel mesoporous MCM-41 aluminosilicate catalyst. *Journal of Catalysis*, 153(1), 25-31.

- [54] Katkar, S., Mohite, P., Gadekar, L., Arbad, B., and Lande, M. (2010). ZnO-beta zeolite mediated simple and efficient method for the one-pot synthesis of quinoxaline derivatives at room temperature. *Open Chemistry*, 8(2), 320-325.
- [55] Mekki, A., Benmaati, A., Mokhtar, A., Hachemaoui, M., Zaoui, F., Habib Zahmani, H., and Boukoussa, B. (2020). Michael addition of 1, 3-dicarbonyl derivatives in the presence of zeolite Y as an heterogeneous catalyst. *Journal of Inorganic and Organometallic Polymers and Materials*, 30(7), 2323-2334.
- [56] Zween, A. F., Shakor, Z. M., and Sherhan, B. Y. (2024). Coke Decomposition Kinetic Model of Spent Hydrodesulfurization catalysts. *Journal of Applied Science Nanotechnology*, *4*, 29-46.
- [57] Yan, J., Jiang, X., Han, X., and Liu, J. (2013). A TG–FTIR investigation to the catalytic effect of mineral matrix in oil shale on the pyrolysis and combustion of kerogen. *Fuel*, *104*, 307-317.
- [58] Al-Iessa, M. S., Al-Zaidi, B. Y., Almukhtar, R. S., Shakor, Z. M., and Hamawand, I. (2023). Optimization of polypropylene waste recycling products as alternative fuels through non-catalytic thermal and catalytic hydrocracking using fresh and spent Pt/Al2O3 and NiMo/Al2O3 catalysts. *Energies*, 16(13), 4871.
- [59] Cowley, M., de Klerk, A., and Nel, R. J. (2005). Amylation of toluene by solid acid catalysis. *Industrial & Engineering Chemistry Research*, 44(15), 5535-5541.
- [60] Al-Kinany, M. C., Al-Megren, H. A., Al-Ghilan, E. A., Edwards, P. P., Xiao, T., Al-Shammari, A. S., and Al-Drees, S. A. (2012). Selective zeolite catalyst for alkylation of benzene with ethylene to produce ethylbenzene. *Applied Petrochemical Research*, 2(3), 73-83.
- [61] Ahmed, R., Sinnathambi, C. M., and Subbarao, D. (2011). Kinetics of de-coking of spent reforming catalyst. *Journal of Applied Sciences*, 11(7), 1225-1230.

DOI: https://doi.org/10.17509/ajse.v6i2.90148 p- ISSN 2776-6098 e- ISSN 2776-5938